



Quantifying Metabolic Heterogeneity in Head and Neck Tumors in Real Time: 2-DG Uptake Is Highest in Hypoxic Tumor Regions

Erica C. Nakajima^{1,2,3}, Charles Laymon⁴, Matthew Oborski⁴, Weizhou Hou⁵, Lin Wang⁶, Jennifer R. Grandis⁷, Robert L. Ferris⁷, James M. Mountz⁴, Bennett Van Houten^{3*}

1 Physician Scientist Training Program, University of Pittsburgh, Pittsburgh, Pennsylvania, United States of America, **2** Howard Hughes Medical Fellow, Howard Hughes Medical Institute, Bethesda, Maryland, United States of America, **3** Department of Pharmacology & Chemical Biology, University of Pittsburgh, Pittsburgh, Pennsylvania, United States of America, **4** Department of Radiology, University of Pittsburgh School of Medicine, Pittsburgh, Pennsylvania, United States of America, **5** Department of Immunology, University of Pittsburgh School of Medicine, Pittsburgh, Pennsylvania, United States of America, **6** Department of Pathology, University of Pittsburgh School of Medicine, Pittsburgh, Pennsylvania, United States of America, **7** Department of Otolaryngology, University of Pittsburgh School of Medicine, Pittsburgh, Pennsylvania, United States of America

Abstract

Purpose: Intratumoral metabolic heterogeneity may increase the likelihood of treatment failure due to the presence of a subset of resistant tumor cells. Using a head and neck squamous cell carcinoma (HNSCC) xenograft model and a real-time fluorescence imaging approach, we tested the hypothesis that tumors are metabolically heterogeneous, and that tumor hypoxia alters patterns of glucose uptake within the tumor.

Experimental Design: Cal33 cells were grown as xenograft tumors (n = 16) in nude mice after identification of this cell line's metabolic response to hypoxia. Tumor uptake of fluorescent markers identifying hypoxia, glucose import, or vascularity was imaged simultaneously using fluorescent molecular tomography. The variability of intratumoral 2-deoxyglucose (IR800-2-DG) concentration was used to assess tumor metabolic heterogeneity, which was further investigated using immunohistochemistry for expression of key metabolic enzymes. HNSCC tumors in patients were assessed for intratumoral variability of ¹⁸F-fluorodeoxyglucose (¹⁸F-FDG) uptake in clinical PET scans.

Results: IR800-2-DG uptake in hypoxic regions of Cal33 tumors was 2.04 times higher compared to the whole tumor (p = 0.0001). IR800-2-DG uptake in tumors containing hypoxic regions was more heterogeneous as compared to tumors lacking a hypoxic signal. Immunohistochemistry staining for HIF-1 α , carbonic anhydrase 9, and ATP synthase subunit 5 β confirmed xenograft metabolic heterogeneity. We detected heterogeneous ¹⁸F-FDG uptake within patient HNSCC tumors, and the degree of heterogeneity varied amongst tumors.

Conclusion: Hypoxia is associated with increased intratumoral metabolic heterogeneity. ¹⁸F-FDG PET scans may be used to stratify patients according to the metabolic heterogeneity within their tumors, which could be an indicator of prognosis.

Citation: Nakajima EC, Laymon C, Oborski M, Hou W, Wang L, et al. (2014) Quantifying Metabolic Heterogeneity in Head and Neck Tumors in Real Time: 2-DG Uptake Is Highest in Hypoxic Tumor Regions. PLoS ONE 9(8): e102452. doi:10.1371/journal.pone.0102452

Editor: Joseph A. Califano, Johns Hopkins Medical School, United States of America

Received: March 29, 2014; **Accepted:** June 2, 2014; **Published:** August 15, 2014

Copyright: © 2014 Nakajima et al. This is an open-access article distributed under the terms of the Creative Commons Attribution License, which permits unrestricted use, distribution, and reproduction in any medium, provided the original author and source are credited.

Data Availability: The authors confirm that all data underlying the findings are fully available without restriction. All relevant data are included within the paper and its Supporting Information files.

Funding: Howard Hughes Medical Institute Medical Fellow (ECN), National Institutes of Health U01CA140230 (JMM), P50CA097190 (JRG & RLF), R01CA077308 (JRG) P30CA047904 (BVH), Pennsylvania Commonwealth Universal Research Enhancement (BVH). The funders had no role in study design, data collection and analysis, decision to publish, or preparation of the manuscript.

Competing Interests: JRG receives funding from Novartis and BMS. None of the authors have any additional conflicts of interests and have nothing to declare with regard to the experiments presented in this study.

* Email: vanhoutenb@upmc.edu

Introduction

Intratumoral heterogeneity is gaining attention as a contributor to tumor recurrence and incomplete response to therapy [1–4]. Fluctuating oxygenation in tumors is well documented [5–13] and oxygen availability is a major determinant of whether glycolytic metabolism or the more efficient oxidative pathways are used for ATP production [14–18]. A tumor's response to variable oxygen levels can lead to metabolic flexibility and type of intratumoral

metabolism, in which lactate produced by hypoxic, glycolytic cells provides a fuel source for oxygenated cells performing oxidative phosphorylation (OXPHOS) [7,17,19,20]. While the elevated glycolytic activity of malignant cells has long dominated the study of cancer metabolism [1,3,21], increasing evidence demonstrates tumors can consume a variety of metabolites such as lactate, glutamine, and fatty acids [5,7,9,11,13,22]. We refer to the ability of cancer cells to alter their nutrient consumption in response to shifting oxygenation as metabolic flexibility. We believe metabol-

ically flexible malignant cells are more likely to form aggressive tumors due to their ability to adapt to environmental pressures.

Tumor hypoxia is a known predictor of worsened prognosis in head and neck squamous cell carcinoma (HNSCC) [14,16,18,23,24]. We believe this outcome is partially due to the metabolic heterogeneity that results from differential oxygenation within a tumor. To our knowledge, a thorough assessment of intratumoral metabolic heterogeneity in HNSCC remains to be performed. While markers of metabolic heterogeneity have been identified in histologic examinations of HNSCC tumors [19,20,25], no studies have mapped metabolic diversity in real-time and *in vivo*, using high resolution fluorescent molecular tomography (FMT). We sought to determine the role of hypoxia in driving metabolic changes in HNSCC tumors.

To validate the metabolic flexibility of HNSCC, we confirmed that hypoxic conditions increased glucose consumption and lactate production in two HNSCC cell lines *in vitro*. The cell line (Cal33) with greater metabolic flexibility was used to grow xenograft tumors. Real-time, *in vivo* fluorescent molecular tomography was performed upon the tumors to measure tumor hypoxia, vasculature, and heterogeneity of glucose uptake. Finally, we extended our findings of xenograft tumor heterogeneity to clinical practice by measuring metabolic heterogeneity in ¹⁸F-fluorodeoxyglucose (FDG) PET-CT scans of four HNSCC tumor patients.

Methods

Tissue Culturing

Cal33, an epidermoid head and neck squamous cell carcinoma cell line derived from an oral squamous cell carcinoma [21,26], was kindly provided by Dr. J.L. Fischel (Centre Antoine Lacassagne, Nice, France). Cell line OSC19 was derived from a squamous cell carcinoma of the tongue [1,22]. Both cell lines were validated using short tandem repeat in April 2011 expanded and frozen down. Cell pellets were kept frozen in liquid nitrogen and newly thawed cells were used from May 2012 to May 2013. Cells were maintained in DMEM containing 25 mM glucose (Gibco) with 10% fetal bovine serum and 1% penicillin-streptomycin at 37°C in a humidified incubator with 5% CO₂, 95% air. Hypoxic culturing was performed in 2% O₂, 7.5% CO₂.

Measuring metabolite consumption and production

Cells were incubated in 21% or 2% O₂ for 12, 24, and 48 hours in culture media described above. At each time point, a media aliquot was harvested and the cell count in each dish was recorded after trypsinization. Concentrations of glucose and lactate in the original and culture media were measured using an Accutrend Plus metabolite meter (Roche) [5,23,24].

Immunoblotting

Cells were lysed on ice immediately after removal from an incubator with TNG cell lysis buffer (Cell Signaling) containing complete Mini protease inhibitor (Roche). Proteins were separated by electrophoresis on Novex 4–12% Bis-Tris gels (Invitrogen), and transferred to nitrocellulose membrane (Bio-Rad). Membranes were blocked in 10% milk in PBS with Tween 20, except when being probed for HIF-1 α , in which case 5% milk TBS solution with Tween 20 was used. The following antibodies were used to probe the membranes: hypoxia inducible factor-1 α (HIF-1 α) (Epitomics, 1:500), lactate dehydrogenase subunit M (LHD-M) (Santa Cruz Biotechnology, 1:1000), pyruvate dehydrogenase kinase 1 (PDHK1) (Cell Signaling, 1:1000), ATP synthase subunit β (ATP5 β) (Abcam, 1:1000), carbonic anhydrase nine (CAIX)

(Abcam, 1:1000), and β -actin (Sigma Aldrich, 1:30,000). Densitometry was performed using ImageJ.

Evaluation of cellular rates of glycolysis and oxidative phosphorylation

The oxygen consumption rate and extracellular acidification rate were recorded in real-time using a Seahorse XF24 Extracellular Flux Analyzer (Seahorse Biosciences) using a slight modification of a previously published protocol [15,25]. See Methods S1 for further method details.

Nude mouse xenograft model

5 \times 10⁵ Cal33 cells were injected subcutaneously into the left flank of 6-week-old female Foxn1 nude mice (Harlan Laboratories) in two sets of experiments with ten mice each. During the first experiment, mice also received an injection of 2.5 \times 10⁵ cells into the right flank. During the second experiment, the mice received 5 \times 10⁵ Cal33 cells into the left flank only. Tumors were palpable after 10 days, and tumors were measured every other day using calipers. The University of Pittsburgh Institutional Animal Care and Use Committee (Pittsburgh, PA) approved all the animal experiments (IACUC protocol: 12070675).

Fluorescent molecular tomography (FMT) and image analysis

Mice were injected intravenously (IV) with 2 nmol of HypoxiSense 680 (PerkinElmer) 48 hours prior to imaging, (Table S1). Mice were injected IV 24 hours later with 2 nmol AngioSense 750 (PerkinElmer) and 10 nmol IRDye-800CW-2-deoxyglucose (IR800-2-DG) (Li-COR Biosciences) (Table S1). 24 hours after the last IV injection, mice were anesthetized with isoflurane, placed into a biplanar imaging cassette, and were imaged in three-dimensions using a VisEn FMT2500 Quantitative Tomography In Vivo Imaging System (PerkinElmer) [26,27]. Slices were acquired with a thickness of 0.25 mm in z-direction. Two dimensional images were created from the FMT DICOM files using ITK-SNAP software [1,6,10]. Each plane represents a 250 μ m thick slice of a tumor. See Materials S2 for further method details.

Anatomical tumor measurement

To validate that the FMT-based ROI was appropriately placed, one mouse was sacrificed immediately after FMT imaging while remaining in the FMT cassette to maintain body position. Using a specialized adapter to hold the FMT cassette, the body underwent MRI scanning with a 7Tesla CliniScan (Bruker Corp.). 3D tumor reconstruction and volume measurement was performed using manually drawn, serial ROIs in ITK-SNAP software.

Immunohistochemistry

Xenograft tumors were excised and flash frozen in OCT (Sakura). One tumor was sectioned while frozen in OCT. The remaining tumors were fixed in formalin, and embedded in paraffin. Before sectioning, a 25-gauge needle was inserted into the tumors to serve as a fiduciary marker. 5 μ m tissue slices were stained for ATP5 β (1:50), CAIX (1:500), HIF-1 α (1:100), and LDH-M (1:250) using the same antibodies as those used for western blotting. Slices were counterstained with hematoxylin. The following positive controls were used, ATP5 β (normal murine kidney), HIF-1 α (normal kidney), LDH-M (normal colon), and CAIX (renal cell carcinoma). A certified pathologist approved the quality of the staining. Slides were scanned at 20 \times on Aperio Imagescope software. Images of whole tumor sections were

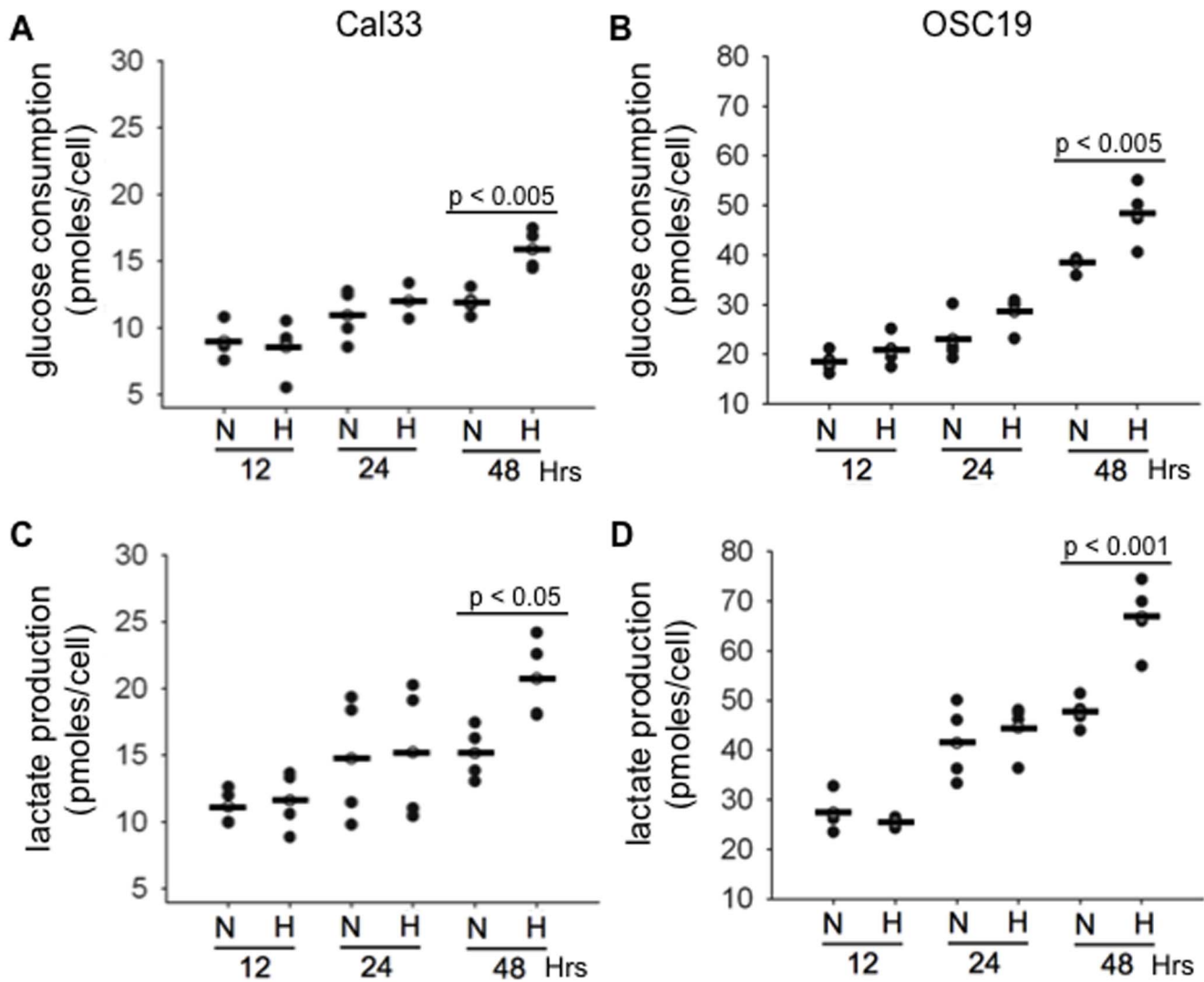


Figure 1. Glucose consumption and lactate production increase under hypoxic conditions. A and B, Cal33 and OSC19 cells consume more glucose after 48 hours of hypoxic culturing than cells grown in normoxic conditions. C and D, a concomitant rise in lactate production was detected in media from Cal33 and OSC19 cells grown in hypoxic conditions for 48 hours. OSC19 cells are more glycolytic than Cal33 cells. Each dot represents one of four replicate dishes used for each time point and culturing condition. The experiment was performed twice with two replicate dishes. P values indicate a significant difference in metabolite concentrations and were calculated using a two-way ANOVA. doi:10.1371/journal.pone.0102452.g001

captured at 20× or 40×. Images of regions within tumor slices were captured at 200×.

A certified pathologist, who was blinded to the FMT imaging results, selected 20 representative regions in two tumors that had shown a strong hypoxic signal and two that had not. The staining intensity was measured by positive pixel count (Aperio version 9). The protein expression was quantified in each region by multiplying the staining intensity by the positive area percentage.

Patients

Four patients with HNSCC tumors gave written consent to be included in this study. None of the patients had received any therapy for their malignancies prior to the baseline positron emission tomography-computed tomography (PET-CT) scan. This protocol was approved by the University of Pittsburgh Institutional Review Board (IRB number PRO09080141).

FDG-PET/CT imaging

PET scans were performed using DST16 PET-CT (GE) that has a spatial resolution of 0.5 cm. Patients fasted for at least four hours prior to receiving 15 mCi ^{18}F -FDG intravenously. For this study, data acquired over the 5-minute interval from 63 to 68 minutes post injection were used in the analysis. A low-dose CT scan without contrast was also acquired for attenuation and scatter correction.

Data were reconstructed iteratively (2 iterations of 28 subsets) following Fourier rebinning (FORE) into a $128 \times 128 \times 47$ (axial) matrix with voxel size $4.7 \text{ mm} \times 4.7 \text{ mm} \times 3.3 \text{ mm}$. Reconstruction was accomplished using the manufacturer's software and included corrections for attenuation, scatter, random coincidences, and deadtime.

Heterogeneity analysis of PET images

Tumor segmentation was standardized across patients using the PETEdge algorithm of the MIMvista software package (MIM

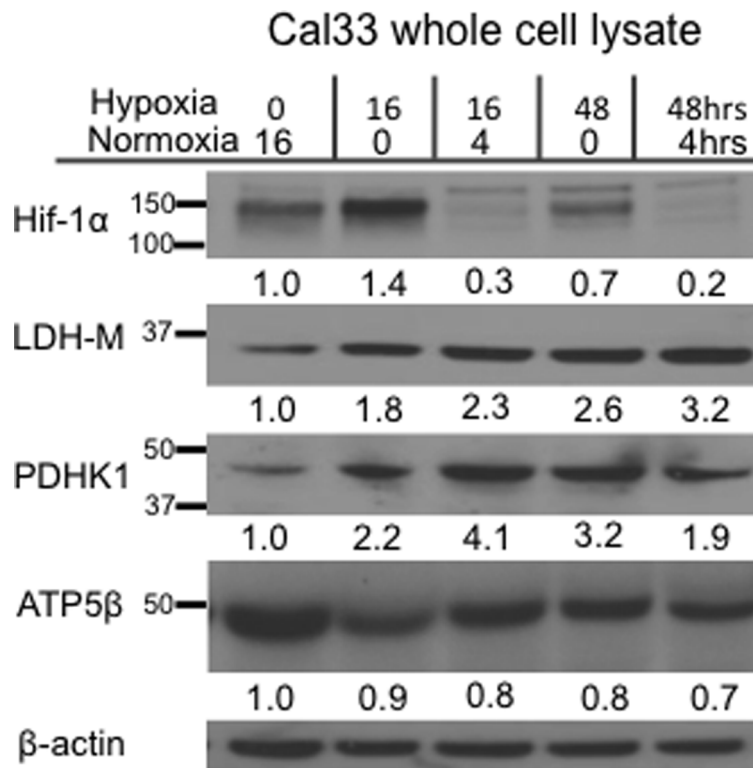


Figure 2. Cal33 exposure to hypoxia leads to increased expression of HIF-1 α , LDH-M, and PDHK1. Western blot analysis of changes in HIF-1 α , LDH-M, and PDHK1 expression in whole cell lysate from Cal33 cultures grown in normoxic (21%), hypoxic (2%), or hypoxic (2%) followed by normoxic (21%) conditions. Cells cultured in 21% oxygen for 16 hours serve as the control for basal protein expression levels. Densitometry values were calculated using ImageJ. Images are representative of duplicate blots.
doi:10.1371/journal.pone.0102452.g002

Software) [5,17]. PETEdge delineates the tumor border in the presence of background signal by assessing changes in ^{18}F -FDG spatial gradients. The PETEdge-drawn ROI was designated as ROI-E.

Quantification in PET is complicated by the modality's limited spatial resolution that results in a blurring of voxel intensities [15,28], a serious challenge for an analysis of heterogeneity. An additional problem is the mixing of background signal into image voxels within the tumor, resulting in an artifactual decrease in apparent tumor signal intensity at the tumor boundary. For the PET scanner used in this study, the spatial resolution is on the order of 0.6–0.7 cm full-width at half-maximum [27,29]. This issue was addressed by contracting the boundary of ROI-E by 0.5 cm circumferentially. The new, contracted ROI is labeled ROI-C. For example, if ROI-E were a sphere of radius 5 cm, then ROI-C would be a sphere of radius 4.5 cm.

The mean ^{18}F -FDG concentration and standard deviation across voxels were calculated within ROI-C. The dimensionless coefficient of variation (CV), defined as the standard deviation divided by the mean, was computed as a measure of heterogeneity.

Results

Hypoxia exposure alters Cal33 cellular metabolism, decreasing OXPHOS and increasing glycolysis

It was imperative to detect HNSCC metabolic flexibility in response to hypoxia *in vitro* prior to the investigation of tumor metabolic heterogeneity *in vivo*. Cal33 and OSC19 cells were

selected for an initial investigation because these lines establish xenografts successfully [6,10,30]. Cal33 and OSC19 cells increased their glucose consumption by 38% ($p < 0.005$) and 26% ($p < 0.005$) respectively, when cultured in 2% O_2 for 48 hours as compared to cultures grown in 21% O_2 (Fig. 1A and B). Both cell lines had a corresponding increase in lactate production after 48 hours of hypoxia exposure (Cal33 37%, $p < 0.05$; OSC19 40%, $p < 0.001$) (Figs. 1C and D). The difference in glucose consumption or lactate production was insignificant at earlier time points of 2% or 21% O_2 culturing. These measurements also demonstrated that OSC19 cells were approximately two and a half times more glycolytic as compared to Cal33 cells in normoxic and hypoxic culturing conditions.

As Cal33 cells showed the greatest increase in glucose consumption after hypoxia exposure, this cell line was selected to assess for altered expression of proteins involved in the metabolic response to hypoxia. HIF-1 α is a transcription factor that regulates acute cellular response to hypoxia [7,9,11,13,15,17]. HIF-1 α was stabilized in Cal33 cells after 16 hours of hypoxia, but was degraded rapidly when cells were maintained in normoxic conditions for four hours after hypoxic incubation (Fig. 2). Expression of HIF-1 α -regulated enzymes lactate dehydrogenase subunit M (LDH-M), and pyruvate dehydrogenase kinase 1 (PDHK1) remained significantly elevated at 16 and 48 hours of hypoxia exposure and after normoxia exposure. These enzymes promote anaerobic glycolysis by shunting carbons away from the OXPHOS pathway. These data support our previous findings of higher glycolytic rate and increased lactate production in Cal33

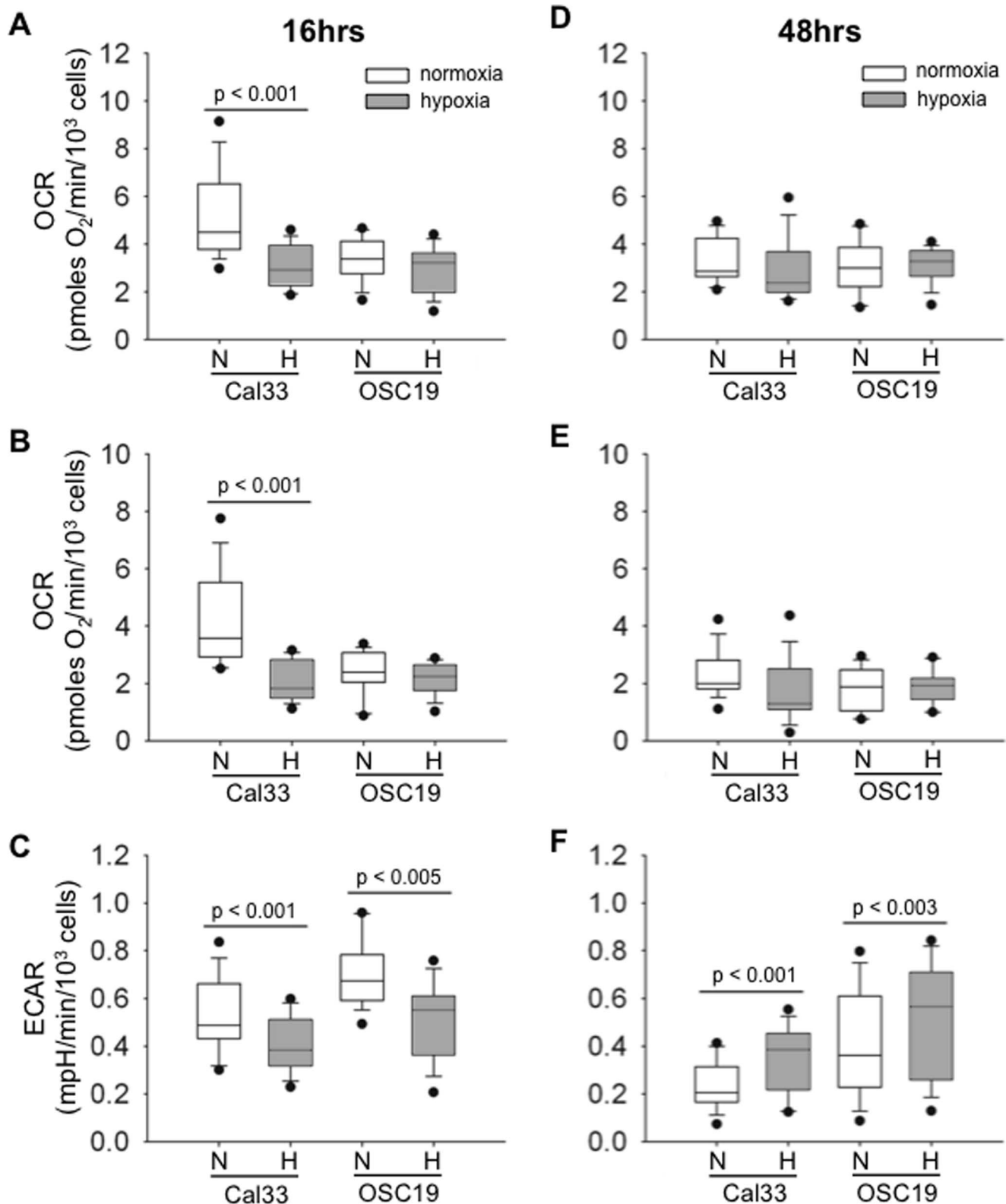


Figure 3. Cal33 cells demonstrate greater metabolic flexibility in response to hypoxia than OSC19 cells. After 16 or 48 hours in 2% (hypoxia) or 21% oxygen (normoxia), 4×10^4 Cal33 or OSC19 cells were plated in a Seahorse XF24 Extracellular Flux Analyzer plate. The Seahorse Analyzer records rates of OXPHOS & glycolysis via the oxygen consumption rate (OCR) and the extracellular acidification rate (ECAR) of each sample culture. A, basal OCR recorded at the assay start after 16 hour incubation. B, ATP-linked OCR is the difference between the basal OCR and the OCR after the addition of oligomycin to sample cultures (see Figure S1). C, Basal ECAR recorded at the assay start. Three experiments were performed at each time point, with five samples per condition. Boxes represent the interquartile range, horizontal lines indicate the median, the T-bars indicate the range, and individual points are outliers. P values were determined by two-way ANOVA. N=normoxia (21% oxygen), H=hypoxia (2% oxygen). D,

Basal OCR recorded at assay start after 48 hour incubation. E, ATP-linked OCR recorded for 48 hour cultures. F, Basal ECAR recorded after 48 hour incubation.

doi:10.1371/journal.pone.0102452.g003

cells cultured in hypoxia for 48 hours (Fig. 1A and C). ATP5 β expression served as an indicator of mitochondrial ATP synthase levels, as the synthase complex is involved in OXPHOS pathway.

ATP5 β expression decreased by approximately two-fold in Cal33 cells exposed to prolonged hypoxia, suggesting that mitochondrial ATP synthase levels drop in response to limited oxygenation.

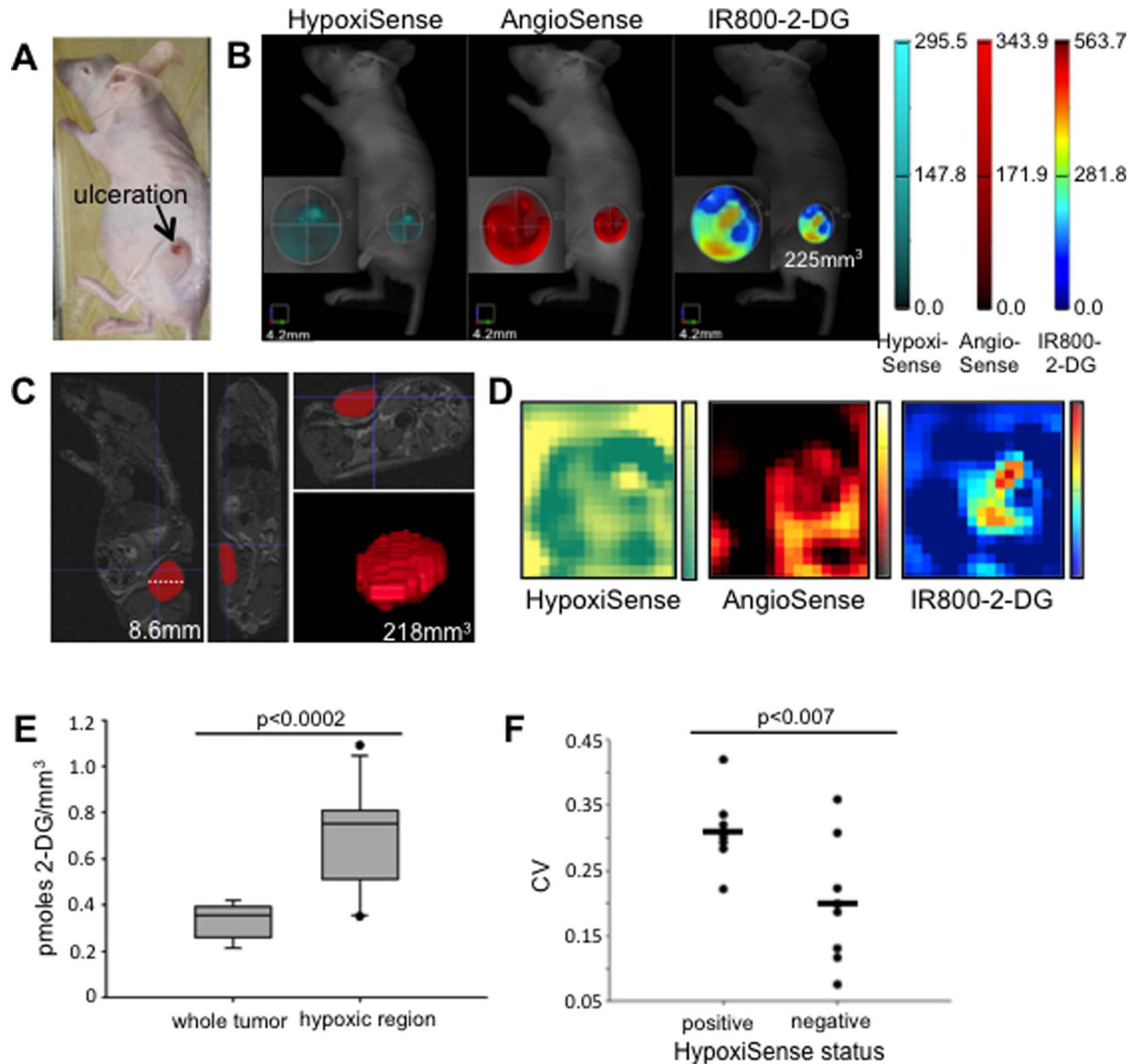


Figure 4. 2-DG uptake in Cal33 xenografts is heterogeneous and is associated with HypoxiSense accumulation. A, Nude mouse with an ulcerated Cal33 xenograft tumor. B, 3D reconstructions of FMT scans capturing HypoxiSense, AngioSense, and IR800-2-DG signal within the xenograft tumor as shown in A. A manually placed ROI measures the tumor volume. C, Anatomic tumor measurement was calculated from MRI slices. Sagittal, axial, and coronal MRI slices of the mouse shown in A and B, with 3D tumor reconstruction. D, two dimensional reconstructions of FMT scans at 2 mm depth within the tumor. E, box plots comparing IR800-2-DG concentration in whole tumors and HypoxiSense-concentrated regions within them (n=8). Boxes represent the interquartile range, the horizontal line indicates the median, the T-bars indicate the range, and individual points are outliers (p, student t-test). F, Tumors were grouped by the presence or absence of HypoxiSense signal within the tumor (n=9 for HypoxiSense positive, n=7 for HypoxiSense negative). The coefficient of variance (CV) for IR800-2-DG concentration within the tumor was calculated (p value was generated using a student's t-test). Each point represents a tumor. Bars indicate the average CV value for the HypoxiSense positive or negative group. doi:10.1371/journal.pone.0102452.g004

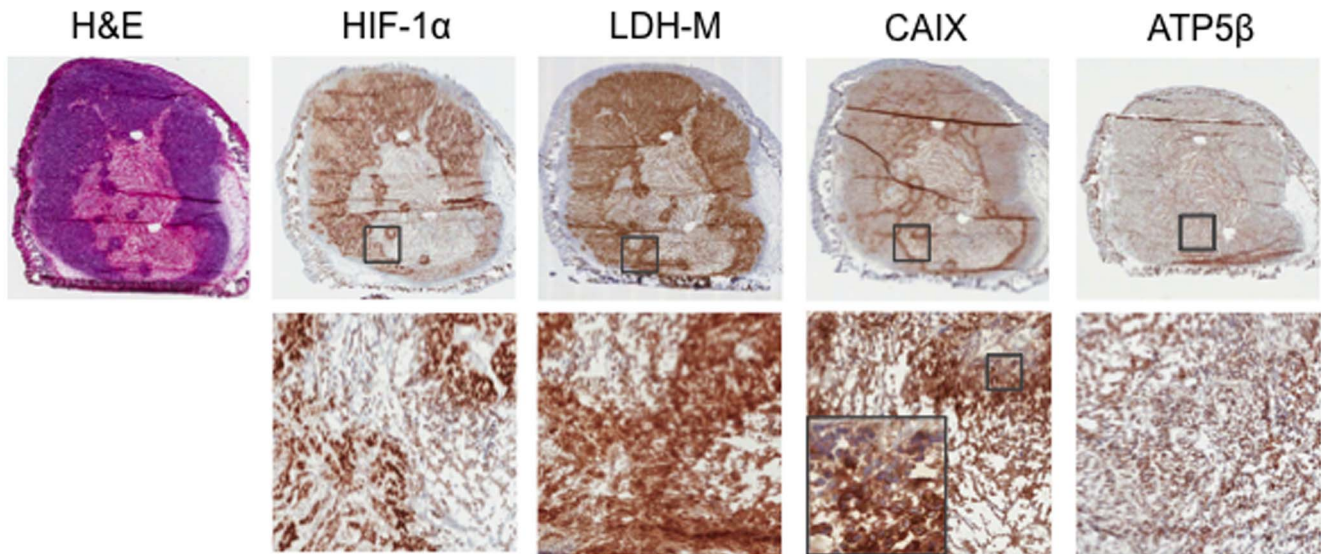


Figure 5. Heterogeneous staining pattern of HIF-1 α , LDH-M, and CAIX expression in xenograft tumors reflects presence of hypoxia. Representative images of HypoxiSense Cal33 tumor sections were probed for HIF-1 α , LDH-M, and CAIX expression by immunohistochemistry (IHC) as described in materials and methods. Gray boxes indicate the region of the tumor shown at 10 \times magnification. Slides were scanned at 20 \times on Aperio Imagescope software. Images of whole tumor sections were captured at 20 \times . Images of regions within tumor slices were captured at 200 \times . Additional inset of CAIX shows cell-surface staining of this protein in peri-necrotic areas. doi:10.1371/journal.pone.0102452.g005

Cal33 cells reduce OXPHOS activity in response to acute hypoxia

Having identified metabolic flexibility and hypoxia-induced increased glycolysis in Cal33 cells, we sought to further validate the glycolytic changes and to determine whether acute hypoxia altered rates of OXPHOS in this cell line. The Seahorse Flux Analyzer assay measures cellular glycolytic and OXPHOS rates simultaneously. The glycolytic rate is measured via changes in the extra-cellular acidification rate (ECAR) of a cell culture. OXPHOS activity is assessed via the oxygen consumption rate (OCR) (Fig. S1). After 16 hour incubation, Cal33 cells cultured in hypoxic conditions demonstrated a dramatic decrease (41%) in their basal OCR as compared to cells cultured in 21% O₂ (Fig. 3A).

The addition of pharmacological inhibitors enables measurements of OXPHOS associated with ATP production (ATP-linked OCR, described in Fig. S1). After 16 hours of hypoxia exposure, Cal33 ATP-linked OCR was reduced by 53% as compared to normoxic treated controls (Fig. 3B). OSC19, the more glycolytic of the cell lines (Fig. 1B), did not demonstrate significant alterations in OXPHOS activity when exposed to hypoxic conditions (Fig. 3A and B). Surprisingly, Cal33 and OSC19 had reduced glycolytic activity after 16 hours of hypoxic culturing (24 and 27% respectively) (Fig. 3C), suggesting that these cells suppressed their glycolytic metabolism initially under reduced oxygen conditions. This would help to explain why we did not detect a significant difference in glucose consumption at earlier time points as shown in Fig. 1.

To confirm the increase in glucose consumption seen at 48 hours in Figure 1, the Seahorse assay was also performed on Cal33 and OSC19 cultures grown in normoxic or hypoxic conditions for 48 hours. Both Cal33 and OSC19 cells revealed increased glycolytic activity (40% and 30% respectively) after 48 hours of hypoxic exposure as compared to cells exposed to normoxic conditions. (Fig. 3F) Interestingly, there was no signif-

icant difference between basal and ATP-linked OCR values for hypoxic and normoxic cultures of both cell lines after 48 hrs of continuous growth under these conditions.

The Seahorse data substantiated the finding that Cal33 are more metabolically flexible than OSC19 cells, displaying lower initial levels of glycolysis and a significant decrease in OXPHOS after hypoxia exposure. As a result, Cal33 was selected as the xenograft model for our *in vivo* investigation of intratumoral metabolic heterogeneity.

Hypoxic tumor regions have increased 2-DG uptake

We next investigated whether discrete regions of Cal33 xenograft tumors had variable glucose uptake, and whether areas of increased glucose uptake would correlate to hypoxic tumor regions. After xenograft Cal33 tumors had grown for approximately two weeks, xenograft-bearing mice were injected with HypoxiSense [26,28], AngioSense [17,29,31], and IR800-2-DG [8,12,30,32], markers of hypoxic tissue, tumor vasculature, and glucose uptake respectively (Table S1). Serial FMT scans recorded intratumoral dye concentration (pmoles/mm³). One tumor had a necrotic ulceration on its surface (Fig. 4A), and this same region contained the strongest HypoxiSense signal in the tumor (Fig. 4B). One mouse underwent whole body MRI scanning immediately after FMT imaging to ensure that the FMT-based tumor size measurements were accurate. The tumor was reconstructed manually in 3D from the MRI slices (Fig. 4C). The FMT-based and MRI-based measurement of the tumor resulted in similar tumor volumes (225 mm³ and 218 mm³, respectively).

Significant heterogeneity in HypoxiSense, AngioSense, and IR800-2-DG tumor uptake was visible from 2D and 3D tumor images (Fig. 4B, D). HypoxiSense was detectable at a set threshold in nine of the 16 tumors imaged, usually within a small focused region of the tumor (Fig. 4B, and Fig. S3). For tumors containing an area of HypoxiSense accumulation, we assessed whether Hypoxisense-positive tumor areas coincided with areas of elevated

Table 1. HIF-1 α , ATP5 β and CAIX expression have greater heterogeneity in HypoxiSense-positive tumors as compared to HypoxiSense-negative tumors.

Hypoxi-Sense status	HIF-1 α			LDH-M			CAIX			ATP5 β		
	Mean	SD	CV	Mean	SD	CV	Mean	SD	CV	Mean	SD	CV
Positive	123.72	27.78	0.22	134.17	10.75	0.08	97.40	31.83	0.33	66.26	12.60	0.19
Positive	69.23	15.78	0.23	148.74	8.73	0.06	138.65	43.32	0.31	51.20	11.42	0.22
Negative	79.30	11.60	0.15	151.01	7.38	0.05	170.69	14.65	0.09	79.9	6.07	0.08
Negative	90.73	17.37	0.19	156.80	6.89	0.04	151.01	7.38	0.05	85.02	10.06	0.12

Mean, standard deviation (SD), and coefficient of variance (CV) of staining were quantified by measuring positive pixel count in 20 representative regions of each tumor slice using Aperio version 9. Quantification of protein expression in each region was calculated by multiplying the staining intensity by the positive area percentage as described in materials and methods.
doi:10.1371/journal.pone.0102452.t001

IR800-2-DG. 3D ROIs were placed around the whole tumor and HypoxiSense-concentrated tumor regions. Three tumors had multiple areas of HypoxiSense accumulation. The IR800-2-DG concentration of the entire eight tumors was compared to the IR800-2-DG concentration in 12 hypoxic regions within those same tumors. The increase in HypoxiSense concentration between whole tumor and hypoxic region ROIs ranged between 2.5 to 225 fold. To compare IR800-2-DG uptake in the whole tumor and HypoxiSense-concentrated regions, these ROIs were then applied to the identical tumor location on the FMT scan of IR800-2-DG. The IR800-2-DG concentration within hypoxic tumor regions was on average 2.04-fold greater than the IR800-2-DG concentration in the whole tumor (Fig. 4E).

We were also interested in whether the degree of IR800-2-DG heterogeneity varied between tumors in which HypoxiSense was detectable and those tumors in which it was undetectable. To achieve this aim, we calculated the coefficient of variation (CV) of IR800-2-DG signal within each tumor by dividing the standard deviation of IR800-2-DG signal by the mean IR800-2-DG signal within each whole-tumor ROI. Intriguingly, those tumors (n = 9) that were strongly positive for HypoxiSense accumulation had an average IR800-2-DG CV value (0.31) that was approximately 33% greater than the CV value (0.2) for tumors in which HypoxiSense was undetectable at the designated threshold (n = 7) (Fig. 4F).

Expression of metabolic proteins associated with glycolysis is heterogeneous in Cal33 xenograft tumors

To confirm our *in vivo* findings of regional hypoxia and metabolic heterogeneity in the xenograft tumors, immunohistochemistry was performed on four tumors to detect HIF-1 α , LDH-M, ATP5 β , and CAIX expression (Fig. 5 and Figure S4). Immunohistochemistry data are presented for one of two tumors that were HypoxiSense positive on FMT. The additional two tumors that were assessed by IHC were HypoxiSense negative (data not shown).

Hematoxylin and eosin staining revealed necrotic tumor centers. HIF-1 α expression was strongest along the necrotic tissue border, suggesting that the tissue breakdown was associated with poor oxygenation. CAIX expression followed a similar pattern, however, the location of the protein expression was additionally informative. CAIX was found at the cell surface of viable tumor cells adjacent to the necrotic areas, while in portions of viable tissue more distant from the necrotic area, CAIX was confined to the cytoplasm. This distinction in CAIX localization explains why CAIX levels appeared unchanged on immunoblotting when Cal33 cells were exposed to 2% oxygen (Fig. S2), as this technique could not discern the location of protein expression. LDH-M expression followed a pattern similar to HIF-1 α , and was strongest in regions of viable tissue surrounded by necrosis. ATP5 β expression was strongest in regions of viable tissue. These patterns of expression were identifiable in the HypoxiSense positive and negative tumors.

To assess the heterogeneity of protein expression in the tumors, 20 representative regions of each tumor section for each of the four tumors, and were scored for positive pixel count. The mean, standard deviation (SD), and CV were calculated from the 20 scores (Table 1). CV values for the expression of HIF-1 α , CAIX, and ATP5 β were higher in the HypoxiSense positive tumors, indicating greater heterogeneity of expression in tumors deemed hypoxic by FMT scan. The CV values of LDH-M expression were similar for HypoxiSense positive and negative tumors.

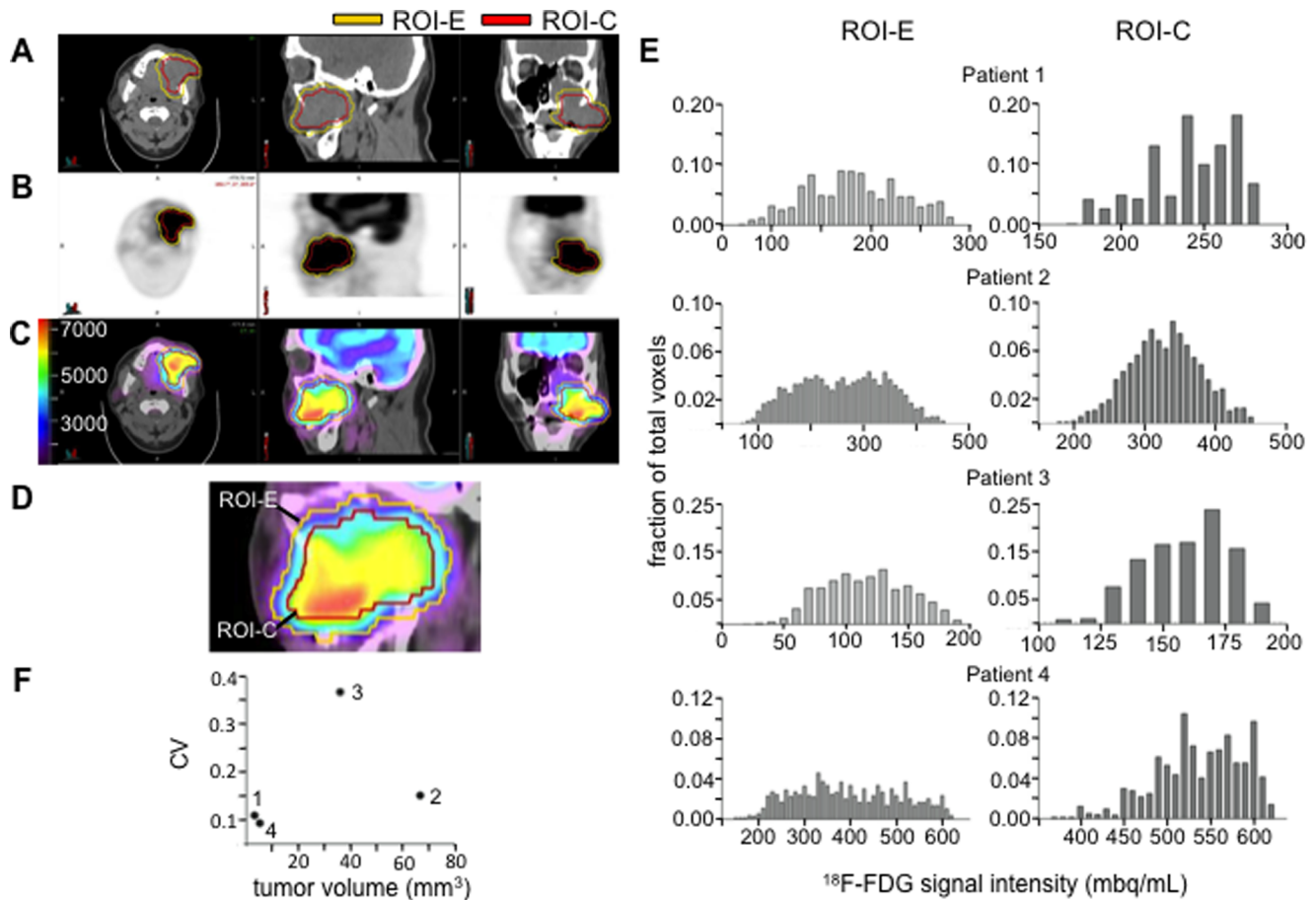


Figure 6. ^{18}F -FDG uptake in human HNSCC tumors is heterogeneous. A, Non-contrast head CT of patient 2. B, ^{18}F -FDG signal on PET scan. C, Fused PET-CT image with scaled color bar (bq/mL). Yellow ROI represents ROI-E, established by PETEdge. Red ROI represent ROI-C, established by contracting ROI-E by 0.5 cm in all directions. D, Histograms of ^{18}F -FDG signal in ROI-E or ROI-C intensity in each tumor. Binning was set at intervals of 10^3 mbq/mL. Mean, maximum, minimum, and standard deviation of ^{18}F -FDG signal within each tumor is shown in Table 2. E, Dot plot comparing tumor volume and coefficient of variance (CV) values established by ROI-C for each tumor. The numbers identify the same tumors numbered to the left of the histograms. Tumor volumes and CVs also listed in Table 2. doi:10.1371/journal.pone.0102452.g006

Measuring intratumoral metabolic heterogeneity in ^{18}F -FDG PET scans

Having identified significant metabolic heterogeneity in a HNSCC xenograft model, we sought to measure metabolic heterogeneity in ^{18}F -FDG PET scans of human HNSCC tumors by assessing CV values of tumor ^{18}F -FDG uptake. The PETEdge function of MIMVista software was used to generate a 3D ROI defining the tumor border (ROI-E). On several occasions, ROI-E encompassed the patient's airway or bone due to spillover of the ^{18}F -FDG signal. Normal tissue surrounding the tumor had lower ^{18}F -FDG signal relative to the tumor, and this difference between tumor and normal tissue would reduce the signal intensity of the adjacent tumor voxels due to partial volume effect [7,9,11,13,15,33,34]. To exclude non-tumor tissue, ROI-E was contracted circumferentially in 3D by 0.5 cm, the value of the PET scanner's resolution, creating ROI-C (Fig. 6A–C). The characteristics and ^{18}F -FDG values recorded by PET-CT for each tumor are shown in Table 2. The intensity value of each voxel in ROI-E and ROI-C was plotted in a histogram to visualize the heterogeneity of ^{18}F -FDG signal within the tumor. These histograms demonstrate that the transformation from ROI-E to

ROI-C consistently removes the tumor regions with the lowest intensity of ^{18}F -FDG signal that are barely above background.

Similar to our assessment of 2-DG heterogeneity within the xenograft tumors, we calculated the CV value of ROI-C of each tumor. While two smallest tumors had the lowest CV values and the larger tumors had higher CV values, Figure 6F shows that tumor volume and CV are do not show a direct correlation. These data suggest that tumor metabolic heterogeneity may not be predictable based upon size alone, and that other factors, such as differential oxygenation and regional differences in cellular metabolomics could be driving tumor metabolic heterogeneity.

Discussion

The purpose of this study was to quantify intratumoral metabolic heterogeneity visually by assessing the variability of 2-DG concentrations within HNSCC tumors. We began our investigation *in vitro* with two HNSCC cell lines that revealed distinct metabolic phenotypes despite being of similar malignant origin. OSC19 cells were highly glycolytic in normal culturing conditions, and hypoxic conditions (2% O_2) stimulated even

Table 2. Tumor characteristics and ^{18}F -FDG-PET values recorded from ROI-C using MIM software.

Patient	Tumor volume (mL)	Max (bq/mL)	Min (bq/mL)	Mean (bq/mL)	Median (bq/mL)	SD (bq/mL)	CV
1	3.19	287489.06	174075.95	246704.23	249721.62	27098.21	0.12
2	66.86	456195.81	155267.7	333665.19	333957.66	50224.01	0.15
3	36.15	261265.5	33070.44	148666.3	142562.28	52314.15	0.37
4	5.18	620795.06	371847.78	542301.38	544443.94	50281.7	0.09

SD, standard deviation. CV, coefficient of variance.
doi:10.1371/journal.pone.0102452.t002

higher levels of glycolysis (Figs. 1 and 3F). OSC19 cells' increased reliance on glycolysis to generate ATP correlated with a lower level of OXPHOS activity at baseline, and an inability to modulate OXPHOS in response to hypoxia. Cal33 cells displayed higher OXPHOS at baseline, but when exposed to hypoxia, this cell line reduced its oxygen consumption in the first 16 hours of hypoxia exposure unlike OSC19 cells (Fig. 3A). After 48 hours of hypoxia exposure, Cal33 cells demonstrated further flexibility of their metabolic phenotype by increasing their glycolytic rate (Fig. 3F). While there was no significant difference in Cal33 OXPHOS activity after 48 hours of culturing in normoxic or hypoxic conditions, we believe this finding is a result of the normoxic cultures adopting slower metabolic activity and proliferation rate as the cellular density increased and nutrients were extracted from the media. Cells cultured in hypoxic conditions for 48 hours were forced to perform glycolysis at a faster rate in spite of increased cellular confluence and nutrient depletion due to the limited oxygen availability. These metabolic changes in Cal33 cells coincided with a rapid increase in HIF-1 α stabilization during acute hypoxia (Fig. 2) and increased expression of PDHK1 and LDH-M after prolonged hypoxia exposure. This robust metabolic flexibility made Cal33 a promising cell line in which to investigate metabolic heterogeneity *in vivo*.

Data presented in Figure 4 indicated that we were able to measure for the first time molecular markers of metabolism and oxygenation simultaneously within live Cal33 xenograft tumors using high-resolution FMT imaging [14,16,18,26,35]. This method revealed regional differences of IR800-2-DG uptake within Cal33 tumors, indicating that portions of the tumors were highly glycolytic, and suggesting that other tumor regions were more reliant upon OXPHOS or other fuel sources. Tumor regions with detectable HypoxiSense accumulation had significantly higher IR800-2-DG signal as compared to the whole tumor, suggesting that the Cal33 cells adapted their metabolism in response to environmental pressures.

Most interestingly, tumors containing detectable HypoxiSense had greater intratumoral heterogeneity of IR800-2-DG signal than those tumors that lacked a hypoxic region as measured by their CV values (Fig. 4). This suggests that hypoxia promotes metabolic heterogeneity within tumors, and that measuring the heterogeneity of glucose uptake within a tumor may serve as a hypoxia marker. This relationship would prove especially valuable if it was present in human HNSCC tumors, as PET is limited to the detection of a single tracer at a time. Rajendran et al. [17,31,36] performed a pixel-by-pixel correlation of ^{18}F -FDG and ^{18}F -labeled fluoromisonidazole (FMISO), a marker of tissue hypoxia, in PET scans of 26 HNSCC tumors as well as several other tumor types. HNSCC tumors had the highest correlation of uptake between the two tracers of all the tumor types, however this relationship was weak. Tumor oxygenation can fluctuate rapidly, and marginal significance of the relationship between ^{18}F -FDG and FMISO could be due to the fact that the PET scans were performed several days apart.

IHC of the xenograft tumors validated the *in vivo* association of greater metabolic heterogeneity in HypoxiSense positive tumors. While HIF-1 α was detected in HypoxiSense negative and positive tumors, heterogeneity of HIF-1 α , CAIX, and ATP5 β expression was consistently greater in HypoxiSense positive tumors. The presence of HIF-1 α and CAIX in HypoxiSense negative tumors suggests that HypoxiSense did not accumulate at a detectable level in these tumors despite the presence of hypoxia. CAIX expression at the cell surface in peri-necrotic tumor regions reflected the pattern of HIF-1 α expression, a finding in agreement with previous studies [8,12,30,32]. While CAIX expression alone has

proven to be an unreliable independent marker of tumor hypoxia [7,33,34,37], the combined expression of CAIX and HIF-1 α was significantly predictive of a worsened prognosis for HNSCC patients [14,16,18,30,35,38]. The variable expression of HIF-1 α and CAIX within a tumor suggests that they may serve as valid biomarkers of intratumoral metabolic heterogeneity.

We extended our investigation of intratumoral heterogeneity to patient samples, and detected ^{18}F -FDG-uptake heterogeneity in HNSCC PET scans of human patients (Fig. 6). Our method of contracting an algorithm-drawn ROI and eliminating 0.5 cm around the perimeter of each tumor aimed to reduce spurious ^{18}F -FDG signal heterogeneity inherent at the tumor edge that arises from the mixing of lower ^{18}F -FDG signal from normal tissues with higher ^{18}F -FDG signal from malignant tissue. We acknowledge that small portions of the tumor may have been excluded from our analysis, however we viewed this trade-off as necessary for a more accurate assessment of the overall tumor metabolic heterogeneity. The largest tumors in our analysis showed the greatest ^{18}F -FDG uptake variability, however as previously noted in Figure 6 the largest tumor did not have the highest variability. A larger study will be necessary to better understand this relationship. Hatt et al [36] examined non-small cell lung cancer, and also concluded that the degree of metabolic heterogeneity was associated with larger tumor size.

While glucose can directly block cellular uptake of IR800-2-DG (data not shown, [30]), there is evidence that uptake and retention of IR800-2-DG and ^{18}F -FDG may not directly coincide. Tseng et al reported that the uptake of ^{18}F -FDG in gastrointestinal stromal xenograft tumors was reduced after treatment with nilotinib, and they regarded this phenomenon as a result of reduced metabolic activity within the treated tumors. Tumor uptake of IR800-2-DG, however, was not seen to decrease significantly after a three day treatment with nilotinib. The authors suggested that the structural differences in these tracers may alter their cellular import and/or retention [37]. IR800-2-DG remains widely used to assess tumor metabolism and follow tumor progression in several cell types [30,38], and its intracellular accumulation has been correlated with GLUT-1 expression [30,39]. While we acknowledge that there may be differences in the mechanisms of dye uptake and retention, our experiments clearly showed a marked heterogeneity in the uptake of this dye in xenograft tumors.

While tumor metabolism is routinely assessed in HNSCC tumors using ^{18}F -FDG PET-CT scans, detecting glucose uptake in relation to hypoxia in HNSCC tumors has been inconclusive [23,24,40,41]. Previous groups have investigated ^{18}F -FDG intratumoral heterogeneity [40,42–45], and our experiments, both *in vitro* and *in vivo*, support further investigation of intratumoral metabolic heterogeneity. We have established a platform for visualizing the consumption of other metabolites and assessing changes in metabolic heterogeneity when tumors are treated with metabolic inhibitors. Recognition of tumor metabolic heterogeneity may lead to improved therapy combinations and outcomes [2,30]. In order to identify combination therapies with the greatest potential efficacy, the forces driving intratumoral heterogeneity

must first be clarified. Differential tumor oxygenation and the variety of metabolites that a tumor can utilize influence tumor growth, and may contribute to the development of metabolically distinct populations. Our studies indicate that variable glucose uptake within a tumor provides information not only about the metabolic capabilities of the tumor, but may also serve as a marker of tumor hypoxia and the ability of tumor cells to respond to environmental pressures. Additionally, our work tested the feasibility of measuring ^{18}F -FDG uptake variability in head and neck tumors on PET scans, which is currently the gold-standard for assessing tumor metabolism. ^{18}F -FDG uptake variability in human tumors may be an indicator of tumor hypoxia, and prognosis, and therefore could guide a patient's treatment regimen. Validation in prospective clinical trials is warranted to translate these findings.

Supporting Information

Figure S1 Seahorse assay records Cal33 and OSC19 glycolytic and oxidative activity.

(TIFF)

Figure S2 Hypoxia exposure does not alter CAIX expression significantly in Cal33 whole cell lysate.

(TIFF)

Figure S3 FMT detection of Hypoxisense, AngioSense, 2-DG in Cal33 xenograft tumors.

(TIFF)

Figure S4 Immunohistochemistry controls.

(TIFF)

Table S1 Fluorescent markers used to identify metabolic heterogeneity *in vivo*.

(TIFF)

Methods S1 Materials S1 describes the evaluation of cellular rates of glycolysis and oxidative phosphorylation using the Seahorse Flux Analyzer. Materials S2 describes the use of the fluorescent molecular tomography (FMT) and image analysis to visualize tumor metabolism *in vivo*.

(TIFF)

Acknowledgments

The authors thank Dr. Sufi Thomas (IACUC and animal training), Marie Acquafondata (IHC) for their contributions to this manuscript. We would additionally like to thank Drs. Richard Steinman and Christopher Bakkenist for their insightful recommendations and editorial reviews.

Author Contributions

Conceived and designed the experiments: ECN CML BVH JRG. Performed the experiments: ECN WH CML MJO. Analyzed the data: ECN CML MJO JMM BVH JRG LW. Contributed reagents/materials/analysis tools: WH JMM RLF JRG. Contributed to the writing of the manuscript: ECN CLM JMM BVH.

References

1. Yushkevich PA, Piven J, Hazlett HC, Smith RG, Ho S, et al. (2006) User-guided 3D active contour segmentation of anatomical structures: significantly improved efficiency and reliability. *NeuroImage* 31: 1116–1128. doi:10.1016/j.neuroimage.2006.01.015
2. Marusyk A, Polyak K (2013) Cancer. Cancer cell phenotypes, in fifty shades of grey. *Science* 339. doi:10.1126/science.1234415
3. Gatenby RA, Gillies RJ (2004) Why do cancers have high aerobic glycolysis? *Nature Reviews Cancer* 4: 891–899. doi:10.1038/nrc1478
4. Davnall F, Yip CSP, Ljungqvist G, Selmi M, Ng F, et al. (2012) Assessment of tumor heterogeneity: an emerging imaging tool for clinical practice? *Insights Imaging* 3: 573–589. doi:10.1007/s13244-012-0196-6
5. Liao S, Penney BC, Wroblewski K, Zhang H, Simon CA, et al. (2011) Prognostic value of metabolic tumor burden on 18F-FDG PET in nonsurgical patients with non-small cell lung cancer. *Eur J Nucl Med Mol Imaging* 39: 27–38. doi:10.1007/s00259-011-1934-6
6. Wheeler SE, Suzuki S, Thomas SM, Sen M, Leeman-Neill RJ, et al. (2010) Epidermal growth factor receptor variant III mediates head and neck cancer cell invasion via STAT3 activation. *Oncogene* 29: 5135–5145. doi:10.1038/onc.2009.279

7. Sonveaux P, Végran F, Schroeder T, Wergin MC, Verrax J, et al. (2008) Targeting lactate-fueled respiration selectively kills hypoxic tumor cells in mice. *J Clin Invest* 118: 3930–3942. doi:10.1172/JCI36843DS1
8. Matsumoto S, Yasui H, Mitchell JB, Krishna MC (2010) Imaging Cycling Tumor Hypoxia. *Cancer Research* 70: 10019–10023. doi:10.1158/0008-5472.CAN-10-2821
9. Wise DR, DeBerardinis RJ, Mancuso A, Sayed N, Zhang X-Y, et al. (2008) Myc regulates a transcriptional program that stimulates mitochondrial glutaminolysis and leads to glutamine addiction. *Proceedings of the National Academy of Sciences* 105: 18782–18787. doi:10.1073/pnas.0810199105
10. Sano D, Myers JN (2009) Xenograft models of head and neck cancers. *Head Neck Oncol* 1. doi:10.1186/1758-3284-1-32
11. Nieman KM, Kenny HA, Penicka CV, Ladanyi A, Buell-Gutbrod R, et al. (2011) Adipocytes promote ovarian cancer metastasis and provide energy for rapid tumor growth. *Nat Med* 17: 1498–1503. doi:10.1038/nm.2492
12. Dewhirst MW, Cao Y, Moeller B (2008) Cycling hypoxia and free radicals regulate angiogenesis and radiotherapy response. *Nature Reviews Cancer* 8: 425–437. doi:10.1038/nrc2397
13. Nakajima EC, Van Houten B (2012) Metabolic symbiosis in cancer: Refocusing the Warburg lens. *Mol Carcinog* 52: 329–337. doi:10.1002/mc.21863
14. Nordmark M, Bentzen SM, Rudat V, Brizel D, Lartigau E, et al. (2005) Prognostic value of tumor oxygenation in 397 head and neck tumors after primary radiation therapy. An international multi-center study. *Radiother Oncol* 77: 18–24. doi:10.1016/j.radonc.2005.06.038
15. Soret M, Bacharach SL, Buwat I (2007) Partial-volume effect in PET tumor imaging. *Journal of Nuclear Medicine* 48: 932–945. doi:10.2967/jnumed.106.035774
16. Bayer C, Kielow A, Schilling D, Maftci C-A, Zips D, et al. (2012) Monitoring PAI-1 and VEGF levels in 6 human squamous cell carcinoma xenografts during fractionated irradiation. *International Journal Of Radiation Oncology Biology Physics* 84: e409–e417. doi:10.1016/j.ijrobp.2012.04.033
17. Denko NC (2008) Hypoxia, HIF1 and glucose metabolism in the solid tumour. *Nature Reviews Cancer* 8: 705–713. doi:10.1038/nrc2468
18. Rajendran JG, Schwartz DL, O'Sullivan J, Peterson LM, Ng P, et al. (2006) Tumor hypoxia imaging with [F-18] fluoromisonidazole positron emission tomography in head and neck cancer. *Clin Cancer Res* 12: 5435–5441. doi:10.1158/1078-0432.CCR-05-1773
19. Ziebart T, Walenta S, Kunkel M, Reichert TE, Wagner W, et al. (2011) Metabolic and proteomic differentials in head and neck squamous cell carcinomas and normal gingival tissue. *J Cancer Res Clin Oncol* 137: 193–199. doi:10.1007/s00432-010-0875-y
20. Rademakers SE, Lok J, van der Kogel AJ, Bussink J, Kaanders JH (2011) Metabolic markers in relation to hypoxia; staining patterns and colocalization of pimonidazole, HIF-1 α , CAIX, LDH-5, GLUT-1, MCT1 and MCT4. *BMC Cancer* 11: 167. doi:10.1038/sj.bjc.6600264
21. Gioanni J, Fischel JL, Lambert JC, Demard F, Mazeau C, et al. (1988) Two new human tumor cell lines derived from squamous cell carcinomas of the tongue: establishment, characterization and response to cytotoxic treatment. *European Journal of Cancer and Clinical Oncology* 24: 1445–1455. doi: 10.1016/0277-5379(88)90335-5
22. Yokoi T, Yamaguchi A, Odajima T, Furukawa K (1988) Establishment and characterization of a human cell line derived from a squamous cell carcinoma of the tongue. *Tumor Research* 23: 43–57.
23. Swiderek H, Logan A, Al-Rubeai M (2008) Cellular and transcriptomic analysis of NS0 cell response during exposure to hypoxia. *Journal of Biotechnology* 134: 103–111. doi:10.1016/j.jbiotec.2008.01.001
24. Devreese K, Leroux-Roels G (1993) Laboratory Assessment of Five Glucose Meters Designed for Self-Monitoring of Blood Glucose Concentration. *Clinical Chemistry and Laboratory Medicine* 31. doi:10.1515/cclm.1993.31.12.829
25. Qian W, Van Houten B (2010) Alterations in bioenergetics due to changes in mitochondrial DNA copy number. *Methods* 51: 452–457. doi:10.1016/j.ymeth.2010.03.006
26. Zhang Q, Yang M, Shen J, Gerhold LM, Hoffman RM, et al. (2010) The role of the intravascular microenvironment in spontaneous metastasis development. *Int J Cancer* 126: 2534–2541. doi:10.1002/ijc.24979
27. Bettinardi V, Danna M, Savi A, Lecchi M, Castiglioni I, et al. (2004) Performance evaluation of the new whole-body PET/CT scanner: Discovery ST. *Eur J Nucl Med Mol Imaging* 31: 867–881. doi:10.1007/s00259-003-1444-2
28. Robey IF, Nesbit LA (2013) Investigating Mechanisms of Alkalinization for Reducing Primary Breast Tumor Invasion. *BioMed Research International* 2013: 1–10. doi:10.1038/nrc2255
29. Nuhrendorf M, Sosnovik DE, Waterman P, Swirski FK, Pande AN, et al. (2007) Dual Channel Optical Tomographic Imaging of Leukocyte Recruitment and Protease Activity in the Healing Myocardial Infarct. *Circulation Research* 100: 1218–1225. doi:10.1161/01.RES.0000265064.46075.31
30. Kovar JL, Volcheck W, Seveck-Muraca E, Simpson MA, Olive DM (2009) Characterization and performance of a near-infrared 2-deoxyglucose optical imaging agent for mouse cancer models. *Analytical Biochemistry* 384: 254–262. doi:10.1016/j.ab.2008.09.050
31. Rajendran JG, Mankoff DA, O'Sullivan F, Peterson LM, Schwartz DL, et al. (2004) Hypoxia and Glucose Metabolism in Malignant Tumors: Evaluation by [18F]Fluoromisonidazole and [18F]Fluorodeoxyglucose Positron Emission Tomography Imaging. *Clinical Cancer Research* 10: 2245–2252. doi:10.1158/1078-0432.CCR-0688-3
32. Hoogsteen IJ, Marres HAM, Bussink J, van der Kogel AJ, Kaanders JHAM (2007) Tumor microenvironment in head and neck squamous cell carcinomas: Predictive value and clinical relevance of hypoxic markers. A review. *Head Neck* 29: 591–604. doi:10.1002/hed.20543
33. Troost EGC, Bussink J, Kaanders JHAM, van Eerd J, Peters JPW, et al. (2005) Comparison of different methods of CAIX quantification in relation to hypoxia in three human head and neck tumor lines. *Radiotherapy and Oncology* 76: 194–199. doi:10.1016/j.radonc.2005.06.031
34. Mayer A, Hockel M, Vaupel P (2005) Carbonic Anhydrase IX Expression and Tumor Oxygenation Status Do Not Correlate at the Microregional Level in Locally Advanced Cancers of the Uterine Cervix. *Clinical Cancer Research* 11: 7220–7225. doi:10.1158/1078-0432.CCR-05-0869
35. Kappler M, Taubert H, Holzhausen H-J, Reddemann R, Rot S, et al. (2008) Immunohistochemischer Nachweis von HIF-1 α und CAIX in fortgeschrittenen Kopf-Hals-Tumoren. Prognostische Rolle und Korrelation mit Tumormarkern und Tumoroxygenierungsparametern. *Strahlenther Onkol* 184: 393–399. doi:10.1007/s00066-008-1813-7
36. Hatt M, Cheze-le Rest C, van Baardwijk A, Lambin P, Pradier O, et al. (2011) Impact of Tumor Size and Tracer Uptake Heterogeneity in 18F-FDG PET and C/T Non-Small Cell Lung Cancer Tumor Delineation. *Journal of Nuclear Medicine* 52: 1690–1697. doi:10.2967/jnumed.111.092767
37. Tseng J-C, Wang Y, Banerjee P, Kung AL (2012) Incongruity of Imaging Using Fluorescent 2-DG Conjugates Compared to 18F-FDG in Preclinical Cancer Models. *Mol Imaging Biol* 14: 553–560. doi:10.1007/s11307-012-0545-3
38. Zhou H, Luby-Phelps K, Mickey BE, Habib AA, Mason RP, et al. (2009) Dynamic Near-Infrared Optical Imaging of 2-Deoxyglucose Uptake by Intracranial Glioma of Athymic Mice. *PLoS ONE* 4: e8051. doi:10.1371/journal.pone.0008051
39. Xie BW, Mol IM, Keereweer S, van Beek ER, Que I (2012) Dual-wavelength imaging of tumor progression by activatable and targeting near-infrared fluorescent probes in a bioluminescent breast cancer model. *PLoS ONE*.
40. Thorwarth D, Eschmann S-M, Holzner F, Paulsen F, Alber M (2006) Combined uptake of [18 F] FDG and [18 F] FMISO correlates with radiation therapy outcome in head-and-neck cancer patients. *Radiotherapy and Oncology* 80.
41. Rajendran JG, Schwartz DL, O'Sullivan J, Peterson LM, Ng P, et al. (2006) Tumor hypoxia imaging with [F-18] fluoromisonidazole positron emission tomography in head and neck cancer. *Clinical Cancer Research* 12: 5435–5441.
42. Qian W, Choi S, Gibson GA, Watkins SC, Bakkenist CJ, et al. (2012) Mitochondrial hyperfusion induced by loss of the fission protein Drp1 causes ATM-dependent G2/M arrest and aneuploidy through DNA replication stress. *J Cell Sci* 125: 5745–5757. doi: 10.1242/jcs.109769
43. Kidd EA, Grigsby PW (2008) Intratumoral metabolic heterogeneity of cervical cancer. *Clinical Cancer Research* 14: 5236–5241. doi:10.1158/1078-0432.CCR-07-5252
44. Tang D, Kang R, Livesey KM, Kroemer G, Billiar TR, et al. (2011) High-mobility group box 1 is essential for mitochondrial quality control. *Cell Metabolism* 13: 701–711. doi:10.1016/j.cmet.2011.04.008
45. van Velden FHP, Cheebsumon P, Yaquib M, Smit EF, Hoekstra OS, et al. (2011) Evaluation of a cumulative SUV-volume histogram method for parameterizing heterogeneous intratumoural FDG uptake in non-small cell lung cancer PET studies. *Eur J Nucl Med Mol Imaging* 38: 1636–1647. doi:10.1007/s00259-011-1845-6